International Journal of Fatigue 202 (2026) 109235

Contents lists available at ScienceDirect

International Journal of Fatigue

journal homepage: www.elsevier.com/locate/ijfatigue

Fatigue crack growth retardation due to crack closure in high-strength steel under high-pressure hydrogen

Aman Arora [a,*], Akinobu Shibata [b], Hisao Matsunaga [a]

[a] Department of Mechanical Engineering, Kyushu University, Fukuoka 819-0395, Japan
[b] Research Center for Structural Materials, National Institute for Materials Science (NIMS), Tsukuba 305-0047, Japan

ARTICLE INFO

Keywords:
Hydrogen embrittlement
Fatigue crack growth
Martensite Steel
Medium manganese low-carbon steel
Crack closure

ABSTRACT

The influence of hydrogen on fatigue crack growth (FCG) was investigated in 90 MPa hydrogen gas using a 3Mn-0.2C martensitic steel with a tensile strength of 1500 MPa. Surprisingly, this steel exhibited significant crack closure in hydrogen gas under specific loading conditions, resulting in considerably lower FCG rates compared to those in air. The roughness- and plasticity-induced crack closure markedly retarded the FCG in hydrogen in a relatively low stress intensity factor regime. However, intrinsic FCG resistance, excluding the effect of crack closure, was indeed degraded by hydrogen. Further analysis revealed that the reduction in cohesive strength of block boundaries depended on the plastic zone size and the inclination angle between the longitudinal axis of the blocks and the macroscopic FCG direction. Consequently, hydrogen-enhanced plasticity-mediated decohesion led to cycle-dependent acceleration of FCG, even in such high-strength steel under high-pressure hydrogen environments.

1. Introduction

In recent years, the pursuit of sustainable energy solutions has intensified the exploration of hydrogen as a clean and efficient fuel source. With the growing demand for hydrogen-powered technologies, the critical need for safe and effective high-pressure hydrogen storage systems is becoming increasingly apparent [1,2,3]. In response, high-strength martensitic steels have emerged as pivotal materials for the development of robust and reliable containment vessels for high-pressure hydrogen storage [4,5].

Martensitic steels, known for their excellent balance of high strength and cost efficiency, are garnering attention due to their unique ability to withstand the demanding conditions of high-pressure hydrogen storage. However, susceptibility to hydrogen embrittlement (HE) necessitates the use of materials that can maintain structural integrity and ensure safety during the storage and transportation processes [6,7,8]. Designing components for high-pressure hydrogen environments requires consideration of various mechanical properties, such as tensile strength, ductility, fatigue life, fatigue crack growth (FCG) rate, and fracture toughness [9,10,11]. Furthermore, to design a HE-resistant microstructure, a comprehensive understanding of the HE mechanisms in different hydrogen-rich atmospheres such as gaseous and electrochemical hydrogen is required [12,13]. Nevertheless, research on the crack resistance of high-strength steels in hydrogen gas remains limited.

Research findings reveal a clear correlation between tensile strength and FCG acceleration in high-pressure hydrogen environments, which is crucial for ensuring structural integrity and reliability. When the tensile strength is below 900 MPa, there is a pronounced acceleration of FCG, reaching 20 to 30 times that in air within a stress intensity factor range of 20 to 30 MPa•$m^{1/2}$ [14,15,16,17]. Notably, this acceleration is classified as “cycle-dependent”, meaning that fatigue life, determined by crack-growth analysis assuming a pre-existing crack, is governed solely by the number of cycles, irrespective of the loading rate. Conversely, for materials with tensile strengths above 900 MPa, hydrogen-induced FCG acceleration exhibits “time-dependent” behavior [14,18,19]. This indicates that the acceleration becomes more pronounced with a decrease in test frequency, rendering fatigue life predictions based on the number of pressurization cycles unreliable. Consequently, traditional fatigue-life design approaches become inapplicable under these conditions.

In this study, to further explore this intricate relationship and obtain fundamental insights necessary for identifying superior high-strength steels for hydrogen applications, a high-pressure (90 MPa) hydrogen gas facility was employed to rigorously test a steel with a tensile strength

* Corresponding author.
E-mail address: amanarora849@gmail.com (A. Arora).

https://doi.org/10.1016/j.ijfatigue.2025.109235
Received 6 June 2025; Received in revised form 28 July 2025; Accepted 9 August 2025
Available online 11 August 2025
0142-1123/© 2025 The Author(s). Published by Elsevier Ltd. This is an open access article under the CC BY-NC license (http://creativecommons.org/licenses/by-nc/4.0/).

of 1500 MPa. This testing aims to gain valuable insights into the behavior of ultrahigh-strength steels, potentially informing future material selection and design strategies for high-pressure hydrogen storage applications.

During this testing, the material examined in the present study exhibited distinctive crack closure, retarding FCG in a low-stress intensity factor regime in high-pressure hydrogen. Generally, FCG may be accompanied by roughness-induced or plasticity-induced crack closure under specific circumstances, thereby affecting FCG behavior [20,21,22,23,24,25,26]. Specifically in a hydrogen environment, it has been observed that hydrogen localizes the plastic deformation at the crack tip, resulting in a shallower plastic wake on the fracture surface [27]. This reduction lowers the crack opening force and increases the effective stress intensity factor (SIF) range (ΔK_{eff}), which in turn leads to smaller crack tip opening displacements (CTODs) at maximum loads compared to those in air. All of these factors contribute to a sharper crack tip and an increased FCG rate. Furthermore, Ritchie et al. [28,29] demonstrated that the increase in FCG rates for Cr-Mo steel in a hydrogen environment is attributed to an increased ΔK_{eff} due to the absence of oxide-induced crack closure. However, in the present study, an unforeseen antagonistic crack closure behavior was observed. Thus, this research also investigated the factors responsible for crack closure in hydrogen environments and correlated these factors with the microstructural features and FCG behavior of the material.

This research contributes to a fundamental understanding of hydrogen-induced cracking and provides practical insights for enhancing the safety and reliability of materials used in high-pressure hydrogen storage systems. To achieve this objective, the effects of hydrogen on FCG and the underlying mechanisms of crack closure were explored through microscopic observations of crack paths and fracture surfaces.

2. Methodology

2.1. Material and specimen

The as-cast ingots, with dimensions of 43 × 43 × 18 mm, were heat-treated as schematically shown in Fig. 1. The material was austenitized at 1100 °C for 30 min in a vacuum, followed by ice-brine quenching (IBQ) and sub-zero cooling in liquid nitrogen (LN_2). The proof strength, $\sigma_{0.2}$, of 1032 MPa and tensile strength, σ_{UTS}, of 1500 MPa were reported for the same material in a previous study [30]. Table 1. shows the chemical composition of the material. The microstructure of the material were analyzed using electron backscatter diffraction (EBSD) on a JEOL JSM-7001F scanning electron microscope (SEM) at an acceleration voltage of 15 kV and a beam step size of 0.25 μm. The material exhibited a fully martensitic microstructure consisting of blocks, packets, and prior austenite grains (PAGs). The average width and length of the blocks were approximately 4.5 μm and 8 μm, respectively. The average diameters of the packets and PAG were approximately 70 μm and 180 μm, respectively.

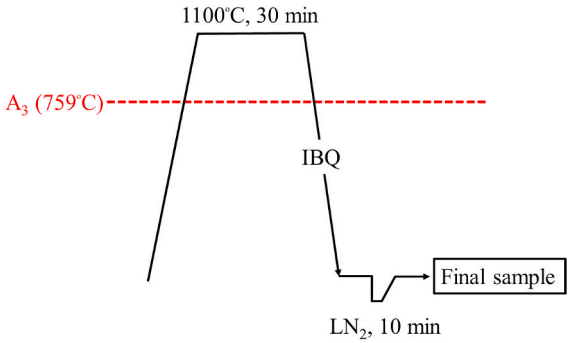


Fig. 1. Schematic illustration of the heat treatment.

The shape and dimensions of the compact tension (CT) specimen used for FCG tests are shown in Fig. 2. The surface of the CT specimen was polished with emery paper and then mirror-finished with a diamond slurry.

2.2. Fatigue crack growth tests and observation of cracks

Two types of FCG tests were conducted at a stress ratio (R) of 0.1 using a sinusoidal waveform, in accordance with the ASTM E647 standard [31]. These experiments were carried out at room temperature in both ambient air and 90 MPa hydrogen gas, using the test facility at HYDROGENIUS. The purity of the hydrogen gas used was greater than 99.999 % (5N), and the hydrogen gas in the chamber was maintained in accordance with ASME KD-10 [32]. To preserve hydrogen purity in the test environment, the chamber was first evacuated and then purged multiple times with the same hydrogen gas used in the test before being pressurized to the target pressure. The hydrogen purity in the chamber was periodically measured after testing. As a result, it was confirmed that the purity of exhaust hydrogen gas met the requirements specified in the aforementioned standard [11].

The first test, referred to as the load-amplitude constant (ΔP-constant) test, established the relationship between the stress intensity factor (SIF) range (ΔK) and the FCG rate (da/dN) under two different test frequencies (f): 5 Hz in air and 1 Hz in hydrogen gas. The second test, known as the ΔK-constant test, was performed at $\Delta K = 10$ MPa·m$^{1/2}$. In this test, f was systematically varied stepwise (1 → 0.1 → 0.01 Hz) for a single specimen. Testing in hydrogen gas commenced immediately after the chamber was pressurized.

Throughout the test, the crack length was continuously monitored using the elastic unloading compliance method with a clip-on gauge attached to the crack-mouth [19,33]. To obtain the amount of crack-growth per cycle (= da/dN), the change in crack length was measured as a function of cyclic load.

After completing both the ΔP-constant and ΔK-constant tests, the specimens were fractured by applying a fatigue load in ambient air. Subsequently, the fracture surfaces were examined using SEM at an acceleration voltage of 15 kV. The roughness profiles and the arithmetic mean roughness of the fracture surfaces were measured using laser profilometry for crack closure analysis.

Additionally, the cross-section of the crack path at the mid-thickness of the CT specimen was observed using EBSD after the ΔP-constant and ΔK-constant tests. For this observation, the CT specimen was bisected along its mid-thickness, and the surface was polished using emery paper, diamond slurry, and colloidal silica suspension to remove any machined layers. The microscopic crack path was then analyzed using EBSD at an acceleration voltage of 15 kV with a beam step size of 0.25 μm.

3. Results

3.1. da/dN- ΔK curves

Fig. 3(a) shows the relationship between da/dN and ΔK as determined from the ΔP-constant tests in air and 90 MPa hydrogen gas. In air, the da/dN-ΔK curves were almost straight on the double logarithmic graph and nearly coincident with each other, following the Paris-Erdogan equation [34].

Surprisingly, the da/dN-ΔK curves for specimens in 90 MPa hydrogen gas did not follow the expected pattern. Generally, hydrogen-induced FCG acceleration is moderate but higher than in air in the lower ΔK regime, and greatly amplified in the higher ΔK regime [14,35,36]. However, in the present study, a peculiar deviation from the linear and increasing trends was observed in the FCG rate in hydrogen. Initially, in the lower ΔK regime, the FCG rate decreases, becoming lower than the FCG rate in air, and then increases. Due to this unconventional FCG behavior, crack closure was analyzed using the method introduced by

Table 1
Chemical composition of 3Mn-0.2C steel.

Element	Mn	C	Si	P	S	Al	N	O	Fe
wt. %	3.02	0.18	0.01	< 0.002	0.001	0.002	0.002	0.001	Bal.

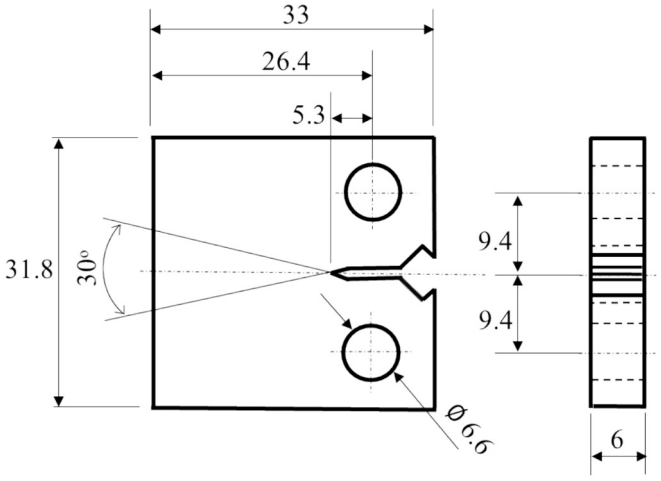


Fig. 2. Shape and dimensions of the CT specimens. All the dimensions are in mm.

Elber [37], which adopts an effective SIF range (ΔK_{eff}) defined by Eq. (1).

$$\Delta K_{eff} = \frac{\Delta P_{eff}}{B\sqrt{W}} \frac{(2+\alpha)}{(1-\alpha)^{3/2}} (0.886 + 4.64\alpha - 13.32\alpha^2 + 14.72\alpha^3 + 5.6\alpha^4) \quad (1)$$

where $\alpha = a/W$, a is the crack length, and W is the width of the CT specimen,

$$\Delta P_{eff} = P_{max} - P_o, \ if \ P_o > P_{min}, \ and \quad (2)$$

$$\Delta P_{eff} = \Delta P = P_{max} - P_{min}, \ if \ P_o < or = P_{min} \quad (3)$$

The crack-opening force (P_o) is an important parameter for studying crack-closure effects. Although various methods exist for verifying and assessing crack closure [38,39,40], in the present study, the unloading elastic compliance method was employed to determine P_o using the load-differential displacement (P-$\Delta\delta$) curve proposed by Kikukawa et al. [41].

Significant crack closure was observed in the specimen tested in hydrogen upon analyzing the crack-opening force (P_o). Fig. 3(b) shows the relationship between da/dN and ΔK_{eff}. Due to the substantial crack closure correction, ΔK_{eff} was used as an intrinsic parameter to quantify the FCG properties. At higher ΔK_{eff}, the FCG rate in hydrogen was four orders of magnitude greater than in air. It is worth noting that no crack closure was observed during the ΔP-constant tests in air or the ΔK-constant test in hydrogen. The factors responsible for the initial crack closure and the accelerated FCG in hydrogen are discussed in Section 4.

3.2. Frequency dependence of crack-growth acceleration

Fig. 4 presents the relative FCG rate, $(da/dN)_H/(da/dN)_{Air}$, as a function of test frequency (f), determined from the ΔK-constant test conducted at $\Delta K = 10$ MPa·m$^{1/2}$ in air and 90 MPa hydrogen gas. Since there was little crack closure during the ΔK-constant test, ΔK is nearly equivalent to ΔK_{eff}. This behavior is markedly different from that observed in the ΔP-constant test. The factors responsible for this difference are discussed in Section 4.

The relative FCG rate in 90 MPa hydrogen gas was approximately 30 times higher than in air. The data points from the ΔK-constant test at $\Delta K = 10$ MPa·m$^{1/2}$ are also shown in Fig. 3(a) and (b). As mentioned earlier, materials with tensile strengths greater than 900 MPa typically exhibit "time-dependent" FCG acceleration at ΔK levels ranging from 20 MPa·m$^{1/2}$ to 30 MPa·m$^{1/2}$. However, this material, with a tensile strength of 1500 MPa, exhibited "cycle-dependent" behavior independent of frequency, although the $\Delta K = 10$ MPa·m$^{1/2}$ applied here is lower than the ΔK levels used in previous studies. It can be readily inferred from the ΔP-constant test (Fig. 2) that, at higher ΔK levels (e.g., $\Delta K =$ 20 MPa·m$^{1/2}$), the FCG acceleration may transition to "time-dependent" behavior, as previously reported in the literature [14,18,19]. This finding is quite interesting and practically important, as it suggests that the present material may be compatible with 90 MPa hydrogen gas if utilized at low ΔK levels. The factors responsible for this behavior are discussed in detail in the following sections through comprehensive analyses of fracture surfaces and EBSD maps of crack paths.

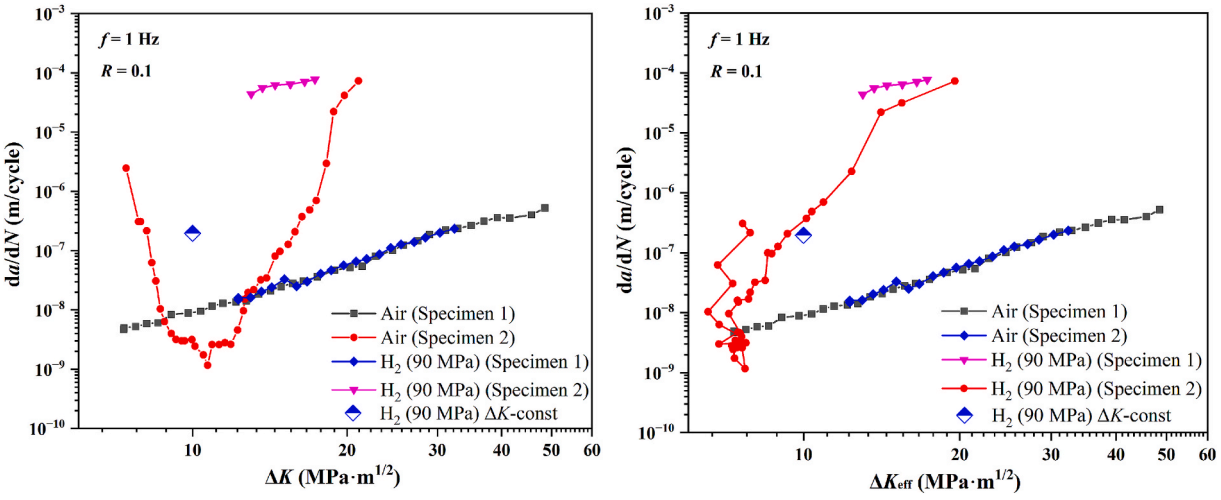


Fig. 3. Relationship between fatigue crack growth rate, da/dN, and (a) stress intensity factor range, ΔK, and (b) effective stress intensity factor range, ΔK_{eff}, for specimens tested in air and 90 MPa hydrogen gas.

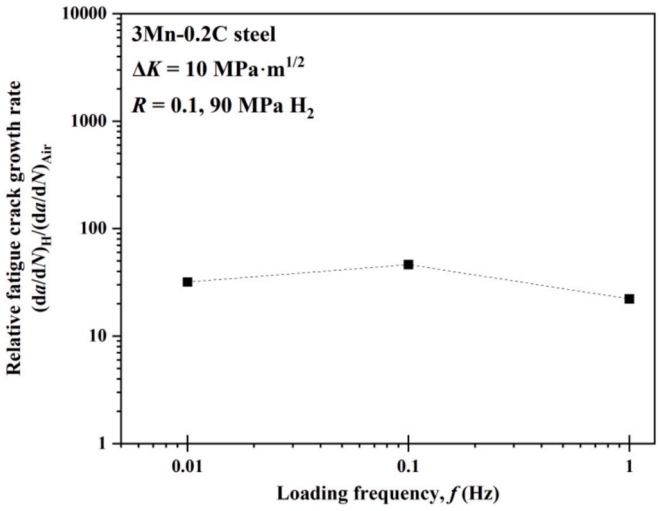


Fig. 4. Relative fatigue crack growth rate, $(da/dN)_H/(da/dN)_{Air}$ as a function of test frequency, f, measured during the ΔK-constant test at ΔK_{eff} ($\approx \Delta K$) of 10 MPa•m$^{1/2}$ in 90 MPa hydrogen gas.

3.3. Fractography

Fig. 5(a) shows an overall view of the fracture surface of the specimen subjected to the ΔP-constant test in air. A transgranular quasi-cleavage (QC) surface is evident at all ΔK levels. Fig. 5(b) and (c) show magnified views of the fracture surface, highlighting finely serrated markings at $\Delta K_{eff} = 7$ MPa·m$^{1/2}$.

Fig. 6(a) and (c) show the crack paths on the front and back surfaces of the specimen in the unloaded condition after the ΔP-constant test in 90 MPa hydrogen gas. It is evident from the figures that a macroscopic kink occurred in the crack path through the thickness during crack propagation. Fig. 6(b) presents an overall view of the fracture surface of the specimen tested in 90 MPa hydrogen gas, showing the pre-crack surface, crack closure surface, and the transition from QC fracture to inter-block (IB) fracture along block boundaries, as well as intergranular (IG) fracture along prior austenite grain boundaries (PAGBs). Such crack kinking is one of the contributing factors to the significant crack closure, which is discussed in Section 4.

Fig. 7 shows the fracture surfaces of specimens tested in 90 MPa hydrogen gas. At $\Delta K_{eff} = 7$ MPa•m$^{1/2}$, QC and IG surfaces are observed (cf. Fig. 7(a)), and a magnified view of the QC region exhibiting river-like patterns is presented in Fig. 7(b). At $\Delta K_{eff} = 10$ MPa•m$^{1/2}$, QC, IB, and IG fracture surfaces are observed (cf. Fig. 7(c)). Fig. 7(d) shows a magnified image of the IB region, revealing distinct step-like features. Notably, the widths of these step-like features closely match the visually-observed block widths in the previous study [30], suggesting that fracture occurred along block boundaries, i.e., an inter-block crack propagation. Additionally, Fig. 7(e) and (f) show the fracture surfaces at $\Delta K_{eff} = 12$ MPa•m$^{1/2}$ and $\Delta K_{eff} = 17$ MPa•m$^{1/2}$, respectively, where IB and IG fractures predominate throughout.

4. Discussion

4.1. Factors responsible for the crack closure

In this section, the factors responsible for crack closure are discussed from the perspective of the crack path and the surface morphology of the crack closure region.

As shown in Fig. 6, during the initial crack propagation at $\Delta K_{eff} \approx 7$ MPa•m$^{1/2}$ in hydrogen, a kink in the crack path increased the roughness of the fracture surface, leading to roughness-induced crack closure [20,21,22]. To verify this, laser profilometry was performed on the fracture surface of specimens subjected to the ΔP-constant test in air and in 90 MPa hydrogen gas. Fig. 8(a) shows the roughness profiles of the fracture surface of the specimen tested in air (cf. Fig. 5(a)). Due to the QC fracture observed throughout the fracture surface, the arithmetic mean roughness, R_a, was approximately 150 μm. Fig. 8(b) and (c) show the roughness profiles of the fracture surface of the specimen tested in 90 MPa hydrogen gas (cf. Fig. 6(b)). The R_a of the QC surface formed in

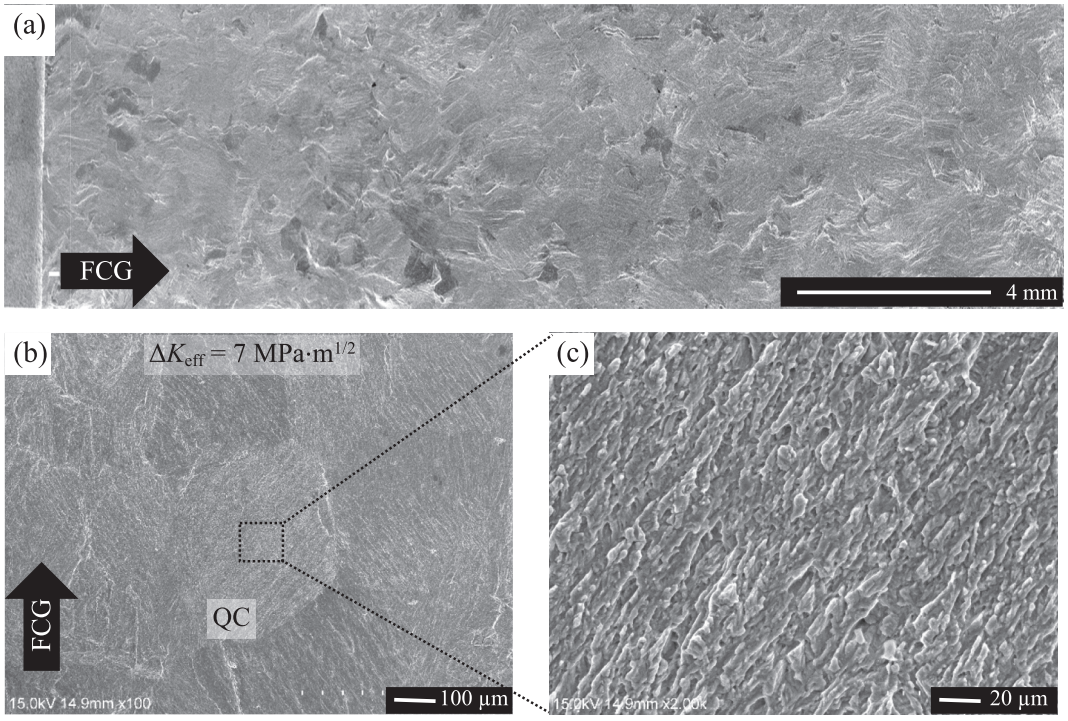


Fig. 5. SEM images of (a) the overall fracture surface of the specimen subjected to the ΔP-constant test in air, (b) the fracture surface at $\Delta K_{eff} = 7$ MPa·m$^{1/2}$, and (c) a magnified view of the fracture surface.

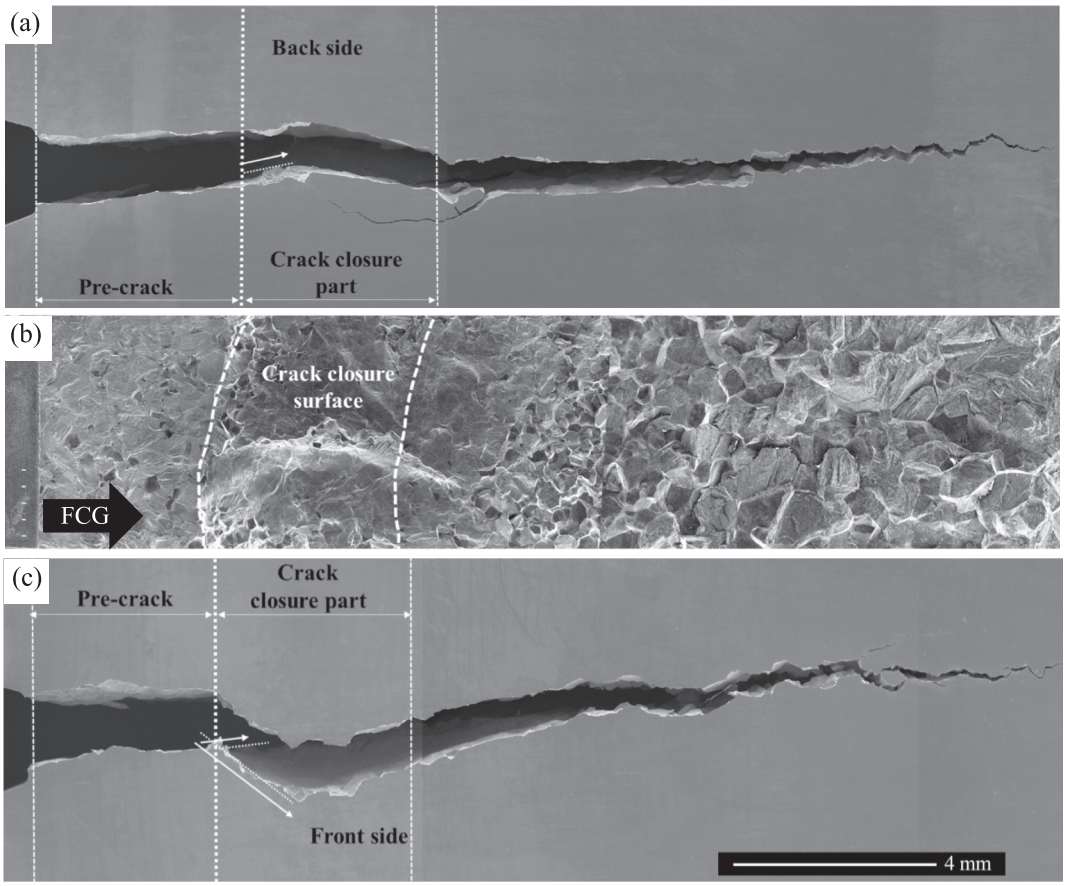


Fig. 6. SEM images of the front (a) and back (c) sides of the specimen in the unloaded state, highlighting the heavily kinked crack paths after the Δ*P*-constant test in 90 MPa hydrogen gas, and (b) the fracture surface.

hydrogen was approximately 1400 μm, roughly ten times greater than that in air. This suggests that in hydrogen gas, the crack propagates along a zig-zag path following the weakest microstructural features deteriorated by hydrogen. Moreover, in hydrogen gas, the average roughness of the crack closure region (QC) is smaller than that of the regions without crack closure, consisting of IB and IG fractures. This implies that crack closure is not solely due to roughness but also requires a mismatch between mating fracture surfaces [21]. It is well-known that hydrogen-related QC fracture is closely associated with plastic deformation [23,24,25]. In QC fracture, shear displacement can enhance the crack-face mismatch, whereas minimal plastic deformation occurs during IG and IB fractures. Thus, it can be concluded that fatigue crack closure results from a combination of roughness and plasticity.

Moreover, it has been suggested that crack closure affects hydrogen-assisted cracking (HAC) [26 42]. When a crack experiences closure, compressive hydrostatic stresses develop near the crack tip. This compressive stress field can significantly influence hydrogen diffusion, a critical factor in HAC. According to Sofronis and McMeeking [43], hydrostatic stress gradients drive hydrogen transport in metals, with tensile stresses promoting hydrogen accumulation and compressive stresses impeding it. Under compressive hydrostatic stress, the hydrogen solubility decreases, reducing the equilibrium hydrogen concentration at the crack tip [44]. Additionally, the compressive stress gradient opposes hydrogen migration toward the crack tip, effectively retarding diffusion [45]. This phenomenon can delay hydrogen embrittlement by limiting the availability of hydrogen at critical locations, thereby slowing crack propagation. Experimental studies by Turnbull et al. [46] on steel specimens confirmed that crack closure mechanisms, such as plasticity-induced shielding, reduce hydrogen uptake at the crack tip due to compressive stresses. Thus, crack closure-induced compressive hydrostatic stress serves as a mitigating factor against HAC, retarding crack growth even under the influence of hydrogen. Therefore, compressive residual stress resulting from initial crack closure in the lower Δ*K* regime is primarily responsible for the retardation of FCG in hydrogen, compared to air. However, in the higher Δ*K* regime, FCG in hydrogen is accelerated relative to air, as expected, and the factors responsible for this acceleration are discussed in the following sections.

4.2. Crack growth along hydrogen deteriorated microstructural features

Fig. 9(a) shows the crack path on the surface of the specimen in the unloaded state after the Δ*P*-constant test in air, and Fig. 9(b) presents the inverse pole figure (IPF) map obtained by EBSD analysis of the marked region in Fig. 9(a). In air, the crack path is relatively straight and transgranular, propagating predominantly through the blocks.

Fig. 9(c) shows the crack path on the surface of the specimen in the unloaded state after the Δ*P*-constant test in 90 MPa hydrogen gas, with the corresponding IPF map for the marked region presented in Fig. 9(d). The IPF maps in Fig. 9(b) and (d) correspond to the same ΔK_{eff} range, clearly revealing the differences in crack morphology. Compared to the specimen tested in air, the crack path in hydrogen exhibits pronounced undulation due to propagation along a zig-zag path following microstructural features deteriorated by hydrogen.

Fig. 9(d) indicates that in the high ΔK_{eff} regime in hydrogen, the crack propagates primarily along PAGBs, with portions of the crack following block boundaries. Numerous studies have shown that strain incompatibility between martensitic blocks, enhanced by hydrogen-induced strain localization, leads to stress concentrations, thereby promoting hydrogen-assisted crack propagation along block boundaries [47,48,49,50]. Therefore, strain incompatibility and the reduction in

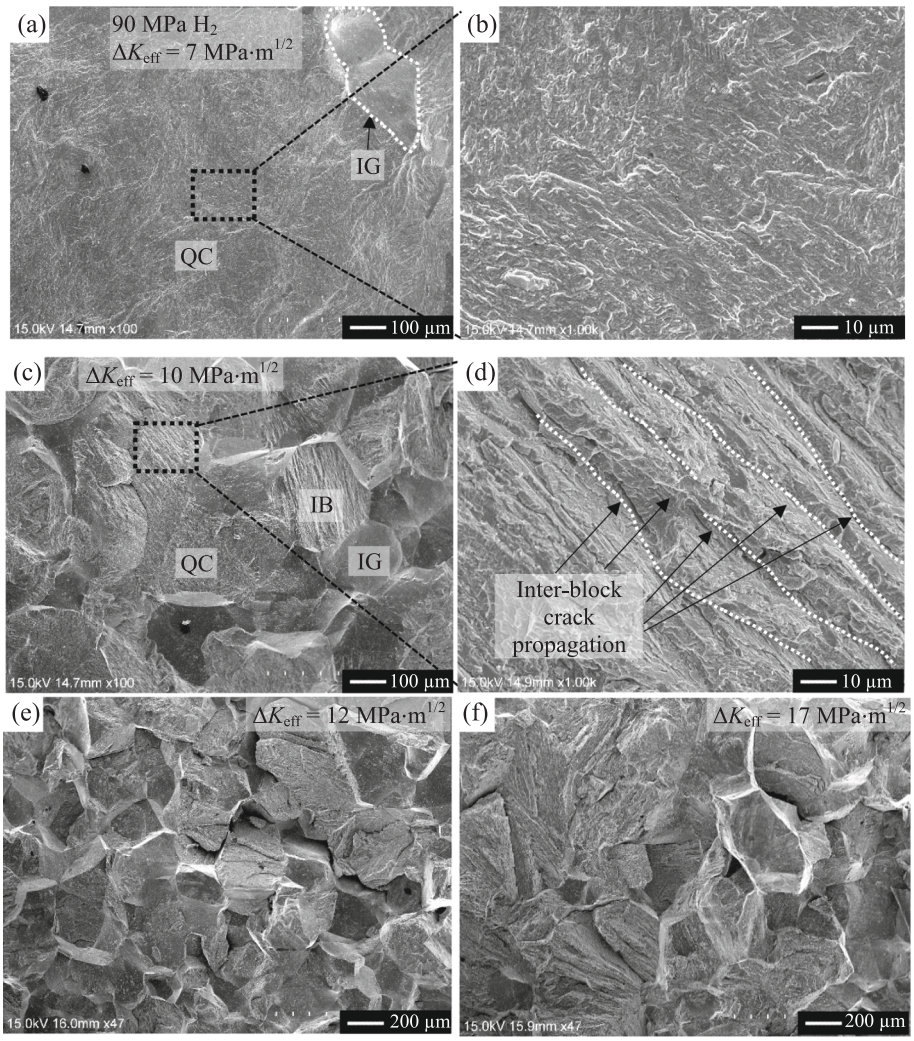


Fig. 7. SEM fractographs of specimens tested in 90 MPa hydrogen gas at (a) and (b) $\Delta K_{eff} = 7$ MPa•m$^{1/2}$, (c) and (d) $\Delta K_{eff} = 10$ MPa•m$^{1/2}$, (e) $\Delta K_{eff} = 12$ MPa•m$^{1/2}$, and (f) $\Delta K_{eff} = 17$ MPa•m$^{1/2}$. In each image, the FCG direction runs from bottom to top.

cohesive strength at PAGBs and block boundaries due to hydrogen are the primary factors contributing to accelerated crack propagation at these specific sites in this material. The potential mechanism responsible for the reduction in the cohesive strength at interfaces, such as PAGBs, is currently under intense debate; however, hydrogen-enhanced decohesion (HEDE) has been proposed and extensively discussed in the literature [51,52,53].

Fig. 10 summarizes the area fractions of different fracture surface morphologies observed on specimens tested in 90 MPa hydrogen. Fig. 10 (a) presents the area fractions of QC, IB, and IG fractures at various ΔK_{eff} levels, while Fig. 10(b) shows these area fractions at different frequencies during the ΔK-constant test conducted at $\Delta K_{eff} = 10$ MPa•m$^{1/2}$. As shown in Fig. 10(a), QC fracture is predominant at lower ΔK_{eff} levels. However, as ΔK_{eff} increases, the fracture mode transitions towards IB and IG. This transition suggests that the decohesion of block boundaries and PAGB is influenced not only by hydrogen but also by the mechanical state ahead of the crack tip, represented by ΔK_{eff}.

To investigate this hypothesis, EBSD analysis was conducted on the crack path of a specimen subjected to the ΔP-constant test in 90 MPa hydrogen at lower ΔK levels, as shown in Fig. 11. The analysis confirmed that in the $\Delta K_{eff} \approx 10$ MPa•m$^{1/2}$ range, the segments exhibiting the IB fracture mode began to increase, corroborating the area fraction trends observed in Fig. 10(a).

For further analysis, assuming small-scale yielding based on Eq. (4), the size of the plastic zone ahead of the crack tip under cyclic loading, Δr_{pl}, can be estimated for plane strain conditions using ΔK_{eff} and the yield stress ($\sigma_y = \sigma_{0.2}$), regardless of the presence or absence of crack closure [24].

$$\Delta r_{pl} = \frac{\Delta K_{eff}^2}{4\pi\sigma_y^2} \tag{4}$$

At $\Delta K_{eff} = 10$ MPa•m$^{1/2}$, Δr_{pl} is approximately 8 μm for this material, comparable to the average block length (see Fig. 12 for the distribution of block lengths). This suggests that when Δr_{pl} is smaller than the average block length, the crack predominantly propagates via QC fracture. As Δr_{pl} approaches the average block length, the fracture mode transitions to IB fracture. However, detailed examination of all the EBSD maps obtained in this study revealed that even at $\Delta K_{eff} \geq 10$ MPa•m$^{1/2}$, IB fracture occurred only when the inclination angle (θ) between the longitudinal axis of the blocks and the macroscopic crack growth direction was less than approximately 38°. Similar dependence of the crack paths on the orientation of blocks, packets, and PAGBs has also been observed in previous studies [54].

The inclination dependence of IB cracking can be analyzed by considering the elastic stress field near the crack tip as the driving force for crack propagation. The distribution of normal stress, σ_θ, near the crack tip in polar coordinates (r,θ) is given by:

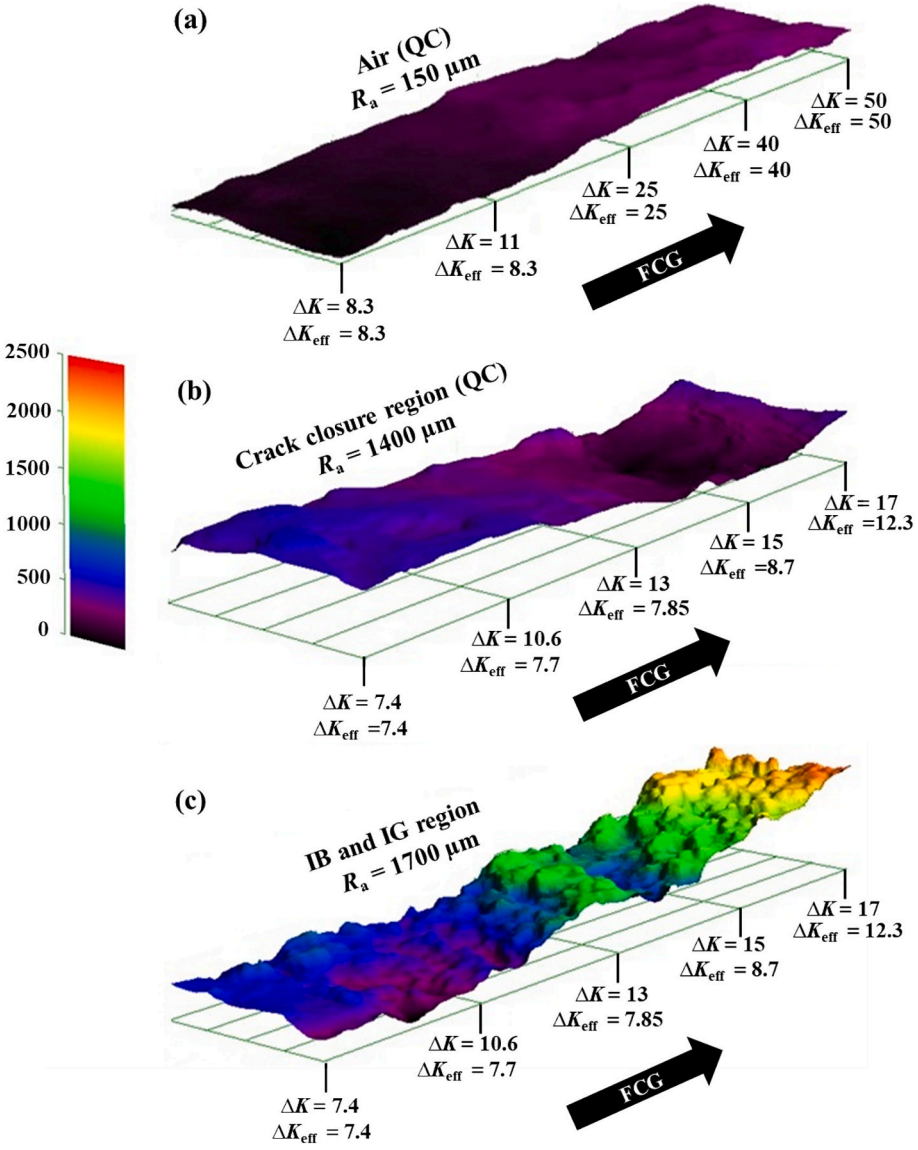


Fig. 8. Laser profilometry of fracture surfaces for specimens tested in (a) air, and (b), (c) 90 MPa hydrogen gas. The unit of SIF range is MPa•m$^{1/2}$.

$$\sigma_\theta = \frac{K_I}{\sqrt{2\pi r}}\left(\frac{3}{4}\cos\frac{\theta}{2}+\frac{1}{4}\cos\frac{3\theta}{2}\right) \quad (5)$$

Fig. 13 shows the distribution of the normalized stress intensity range at the crack tip, $\Delta\sigma_\theta\sqrt{2\pi r}/\Delta K_I$, as a function of the inclination angle (θ) based on Eq. (5). Particularly within the range $|\theta| \leq 38°$, the normalized stress intensity range is notably high, which can enhance the decohesion of block boundaries. Additionally, Fig. 14 shows the variation of fracture modes observed in hydrogen as a function of the absolute inclination angle of blocks relative to the macroscopic FCG direction ($|\theta|$) and ΔK_{eff}.

The favorable conditions for IB crack propagation occurs when the cyclic plastic zone size is comparable to or greater than the average block length (i.e., $\Delta r_{pl} \geq 8$ μm), at $\Delta K_{eff} \geq 10$ MPa•m$^{1/2}$, and $|\theta| \leq 38°$. Due to the higher probability of favorable conditions for IB near $\Delta K_{eff} =$ 10 MPa•m$^{1/2}$, the fracture mode transitioned from QC to IB. As the plastic zone size further increases, a competition arises between favorable conditions for IB fracture and the presence of PAGBs near the crack tip. Consequently, at higher ΔK_{eff} values, both IB and IG fracture modes dominate, as shown in Figs. 7, 10, and 14.

It has been reported in several studies that the fatigue crack growth rate and fracture mode in metallic materials change around the ΔK level where the plastic zone size becomes comparable to the grain size [55,56]. However, the exact mechanisms by which the relative dimensions of these two features influence crack propagation remain unclear. In this study, the plastic zone size was selected as a measure of the extent of plastic deformation at the crack tip, and the average block length was chosen as a representative microstructural length scale for comparison. Although this point will be briefly revisited in later sections, the underlying mechanisms governing their competition merit further detailed investigation.

4.3. Cycle-dependent fatigue crack growth

As mentioned in the Introduction, commercial-grade low-alloy steels with a martensitic structure and tensile strengths exceeding 900 MPa exhibit a "time-dependent" acceleration of hydrogen-enhanced FCG in the relatively high ΔK regime (e.g., $\Delta K_{eff} = 20$ to 30 MPa•m$^{1/2}$). In the ΔK-constant test at $\Delta K_{eff} = 10$ MPa•m$^{1/2}$, the present material exhibited cycle-dependent acceleration (cf. Fig. 4), where the amount of crack growth per cycle was independent of loading frequency. It should be noted that this material would also exhibit time-dependent acceleration at higher ΔK levels (e.g., $\Delta K > 20$ MPa•m$^{1/2}$).

Setoyama et al. [19] interpreted the time-dependent FCG observed in

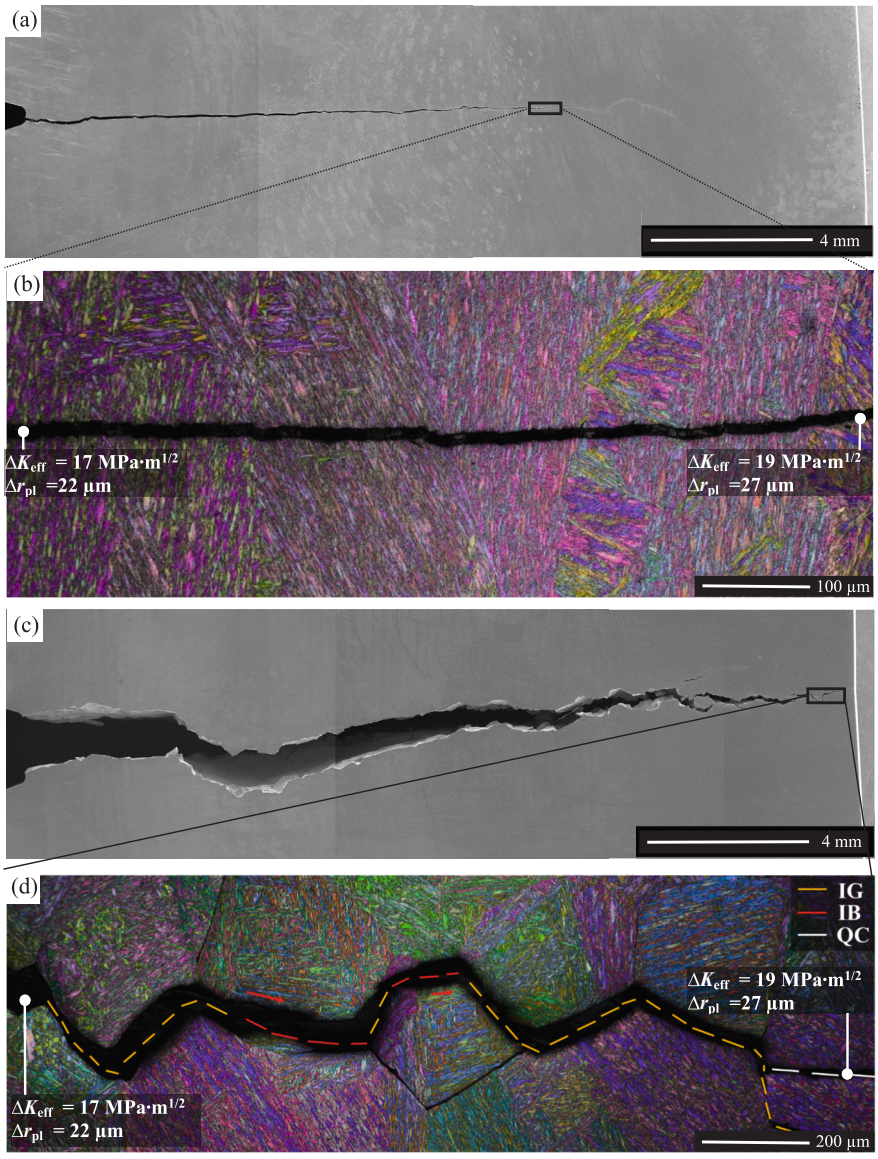


Fig. 9. Crack paths and corresponding IPF maps obtained via EBSD analysis for specimen subjected to the Δ*P*-constant test: (a) crack path on the surface of the specimen tested in air, with (b) the corresponding IPF map of the area indicated by the black rectangle. (c) Crack path on the surface of the specimen test in 90 MPa hydrogen, with (d) the corresponding IPF map of the area indicated by the black rectangle; red arrows denote the orientations of the blocks.

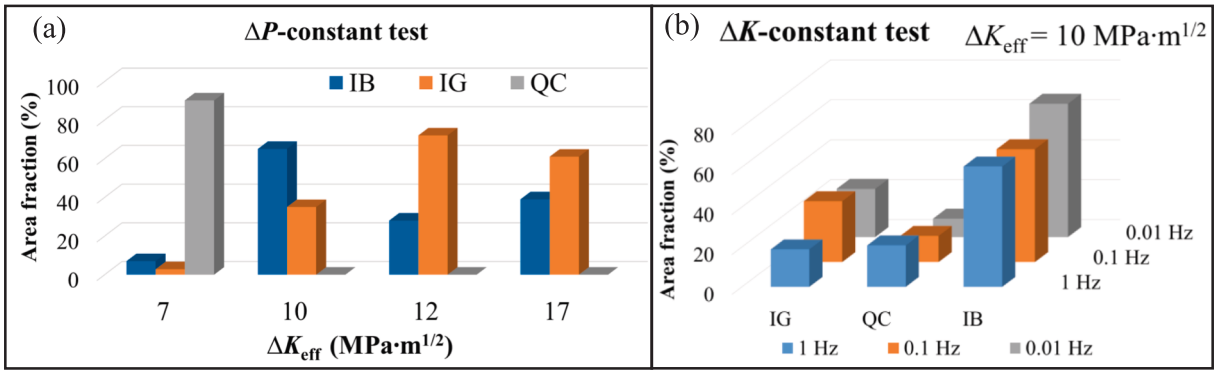


Fig. 10. Area fractions of quasi-cleavage (QC), inter-block (IB), and PAGBs (IG) fracture modes observed on the fracture surface of specimens tested in 90 MPa hydrogen: (a) as a function of ΔK_{eff} under Δ*P*-constant test conditions; (b) as a function of test frequency at ΔK_{eff} = 10 MPa•m$^{1/2}$ under Δ*K*-constant test conditions.

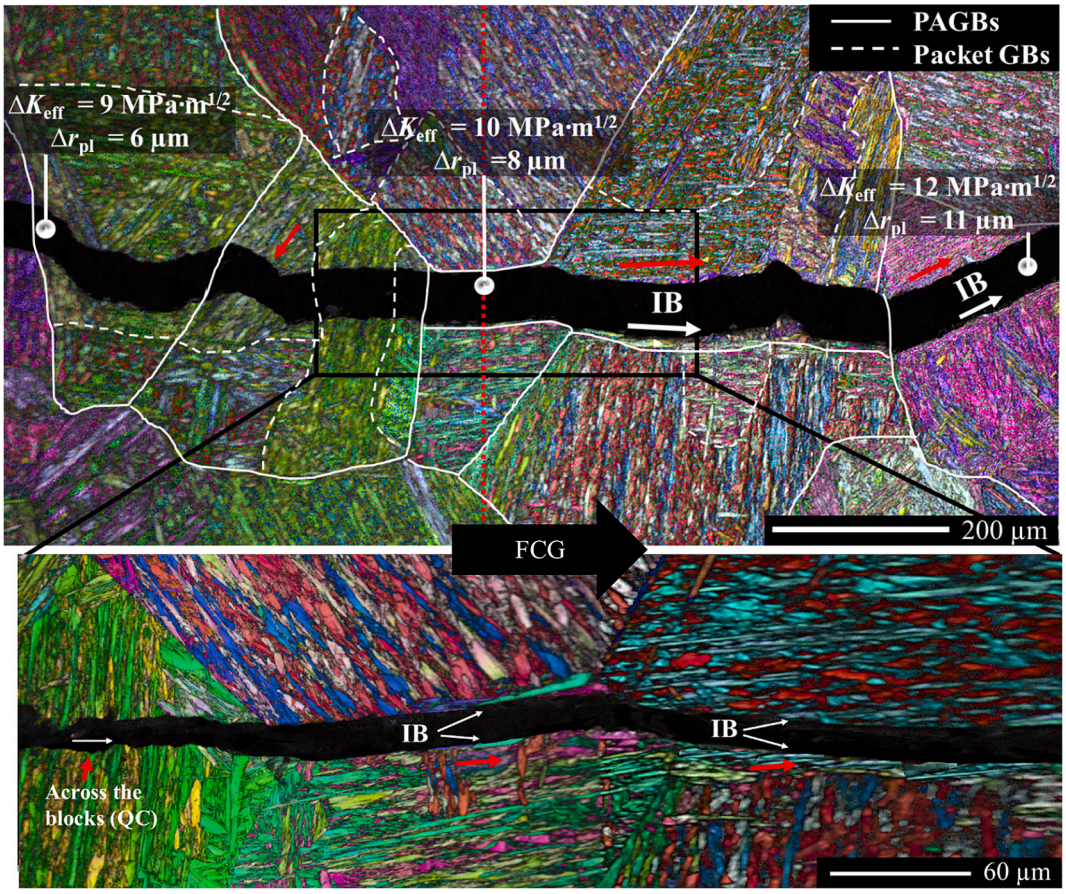


Fig. 11. IPF map showing the FCG path in the specimen tested in 90 MPa hydrogen, from ΔK_{eff} = 9 MPa•m$^{1/2}$ to ΔK_{eff} = 12 MPa•m$^{1/2}$. The map illustrates QC fracture and its transition to IB fracture at $\Delta K_{eff} \approx$ 10 MPa•m$^{1/2}$. Red arrows indicate the orientations of the blocks.

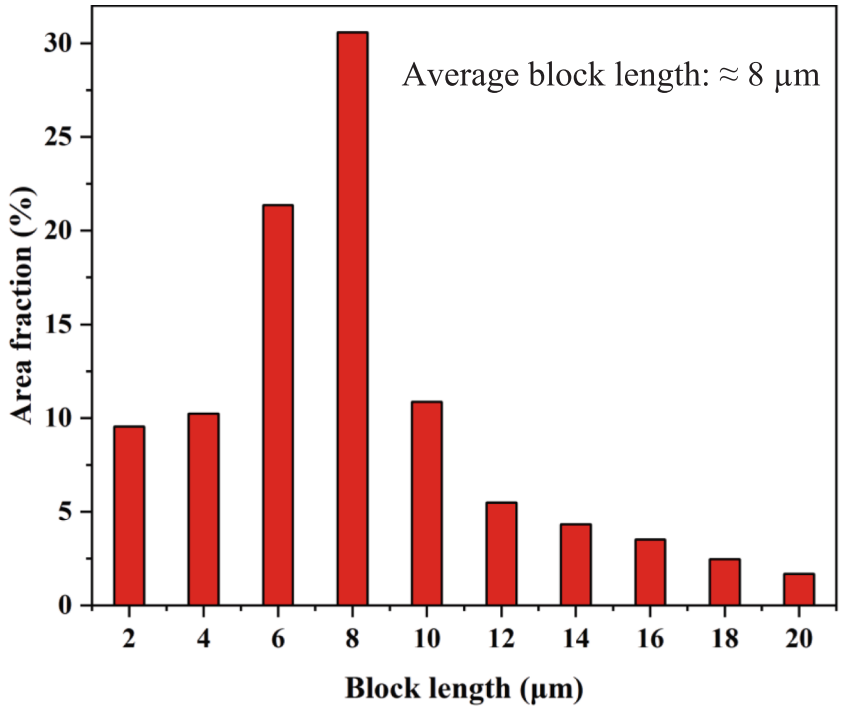


Fig. 12. Distribution of the block length.

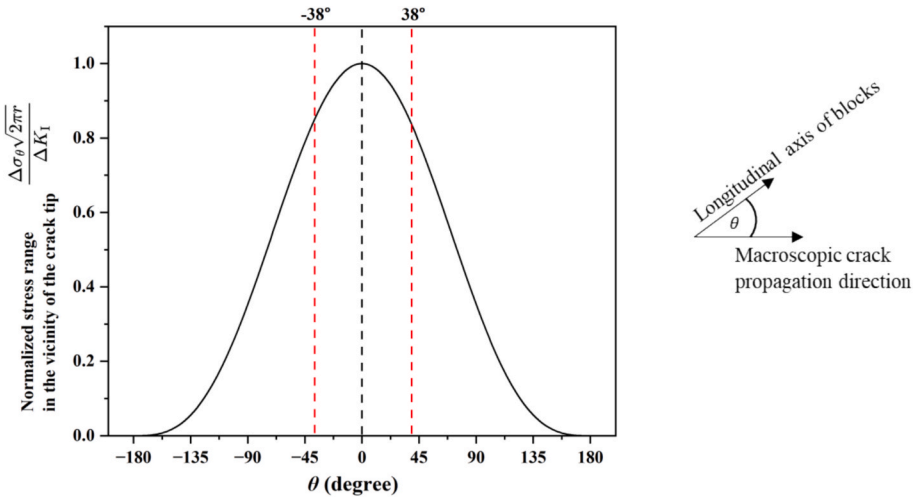


Fig. 13. Distribution of normalized stress range at the crack tip as a function of the inclination angle (θ) of the blocks relative to the macroscopic crack growth direction.

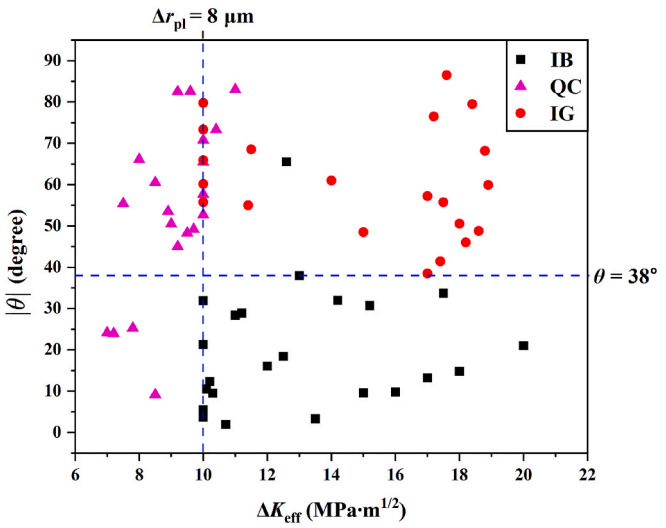


Fig. 14. Variation of fracture mode with the absolute inclination angle of blocks relative to the macroscopic crack growth direction ($|\theta|$), plotted against ΔK_{eff}.

0.4 %C Cr-Mo steel, JIS-SCM440, at ΔK = 30 MPa•m$^{1/2}$ as resulting from competition among the strengths of different boundaries ahead of the crack tip. They noted that if the local driving force (e.g., normal stress) exceeds the fracture resistance of microstructural boundaries ahead of the crack tip (e.g., critical normal stress for fracture along PAGBs, block, and packet boundaries), these boundaries will fracture. Furthermore, the combination of the tensile stress field ahead of the crack tip and stress-induced hydrogen diffusion causes the crack growth per cycle to become proportional to the loading duration, thus exhibiting time-dependent behavior.

However, the cycle-dependent FCG in the present material at ΔK_{eff} = 10 MPa•m$^{1/2}$ is attributed to the dominance of the IB fracture mode over the QC and IG modes. This suggests that the block boundaries segregated with hydrogen atoms acted as the weakest link in determining the crack path. Although the exact mechanism has yet to be established, it may involve a reduction in the local yield strength due to hydrogen-enhanced plasticity [57] in combination with hydrogen-enhanced decohesion (HEDE) [52,58].

When the material can accommodate displacement or crack advancement through plastic deformation—either by directly or indirectly promoting dislocation emission ahead of the crack tip [59,60,61,62], or by any HE mechanism [63,64,65] dominating the FCG—the driving normal stress does not exceed the fracture resistance of microstructural boundaries, resulting in FCG independent of loading duration or frequency. Furthermore, under favorable conditions influenced by hydrogen ($\Delta r_{pl} \geq 8$ μm and $|\theta| \leq 38°$), the crack predominantly propagates via decohesion of block boundaries.

This implies that when the plastic zone becomes sufficiently large around $\Delta K_{eff} > 10$ MPa•m$^{1/2}$, to encompass the average block length, localized plasticity initially occurs due to hydrogen segregation at block boundaries. Subsequently, decohesion of block boundaries occurs once the normal stress acting on the inclined block becomes sufficient to cause fracture. Therefore, through the hydrogen-enhanced plasticity-mediated decohesion mechanism responsible for IB fracture [66], this material exhibits cycle-dependent FCG acceleration.

Fig. 15(a) and (b) present schematics of the FCG process at ΔK_{eff} = 10 MPa•m$^{1/2}$ in air and hydrogen gas, respectively, illustrating hydrogen-assisted crack propagation along block boundaries with different inclination angles. Fig. 15(c) shows the IPF map obtained from the mid-section of the specimen tested in hydrogen, revealing typical IB crack propagation.

In summary, crack closure due to roughness and plasticity positively contributes to the retardation of FCG in high-pressure hydrogen. It is evident that the cyclic plasticity ahead of the crack tip, combined with the hydrogen-enhanced plasticity-mediated decohesion of block boundaries, plays a crucial role in determining the cycle-dependent behavior in steels with strengths around 1500 MPa. Furthermore, the reduction in the cohesive strength of PAGBs due to hydrogen-enhanced decohesion (HEDE), along with IB fracture accelerates the FCG in high-pressure hydrogen. Interestingly, hydrogen-induced degradation of block and packet boundaries causes stress-driven/time-dependent FCG in JIS-SCM440 (0.4 %C Cr-Mo) steel [19] but not in this (3Mn-0.2C) steel. It should be noted, however, that in the ΔK-constant test, the ΔK level for this (3Mn-0.2C) steel is lower (e.g., ΔK = 10 MPa·m$^{1/2}$) than that for JIS-SCM440 (0.4 %C Cr-Mo) steel (e.g., ΔK = 20 MPa·m$^{1/2}$). Therefore, future research should investigate the influence of potential factors (e.g., chemical composition, microstructure, and loading conditions) on the microscopic mechanisms responsible for hydrogen-induced degradation of block boundaries.

5. Conclusions

A steel alloy containing 3% Mn and 0.2% C, with a tensile strength of 1500 MPa, underwent fatigue crack growth (FCG) tests in both air and in

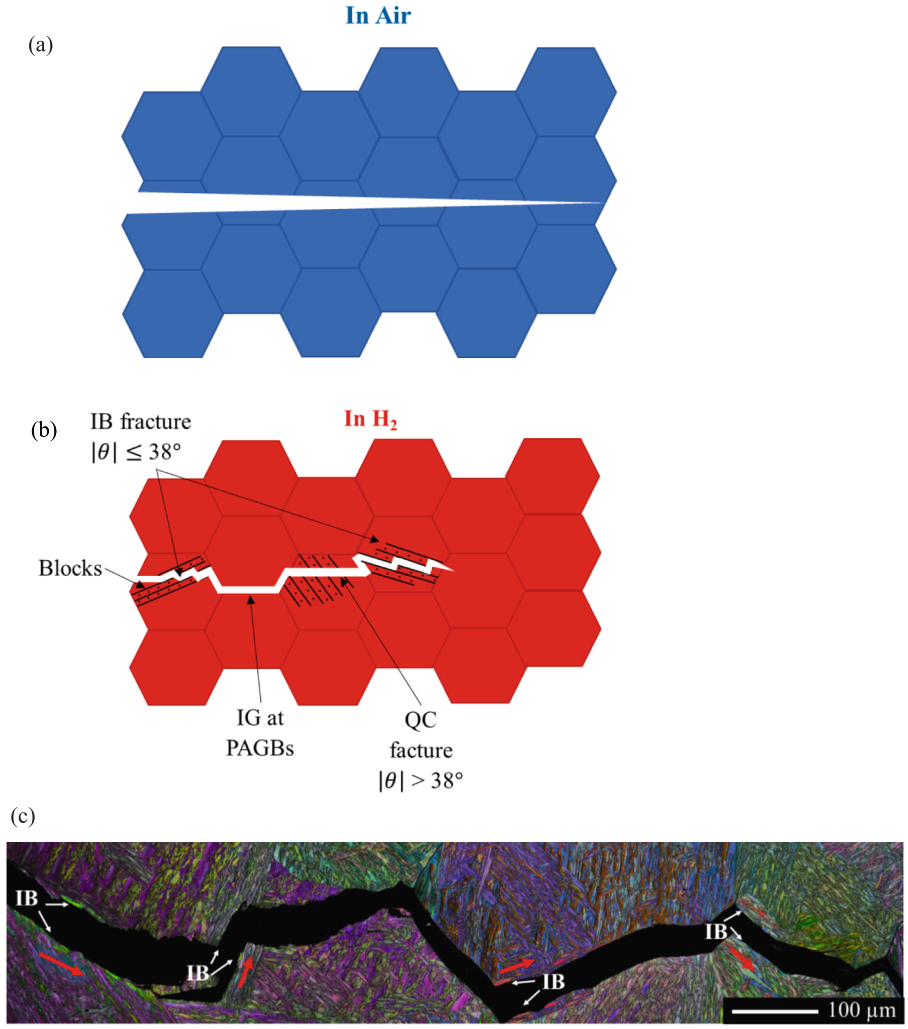


Fig. 15. Schematics comparing FCG in (a) air and (b) 90 MPa hydrogen gas. (c) IPF map of the specimen tested at $\Delta K_{eff} > 10$ MPa•m$^{1/2}$ in 90 MPa hydrogen gas, showing cracks propagating along block boundaries (IB). Red arrows indicate the inclination of the blocks.

90 MPa hydrogen gas. The results revealed an initial notable deceleration due to crack closure, followed by significant FCG acceleration in hydrogen gas. At a ΔK_{eff} of 10 MPa·m$^{1/2}$, the acceleration rate in the material was found to be insensitive to loading frequency, despite its very high strength.

After thorough examinations of fracture surfaces, crack paths, and mechanical states ahead of the crack tip, the following conclusions regarding the mechanism of cycle-dependent FCG acceleration were drawn:

1. Scanning electron microscopy observations of the crack path and laser profilometry of the fracture surfaces revealed that fatigue crack closure results from a combination of fracture surface roughness and crack-tip plasticity, leading to significant FCG retardation in the lower ΔK regime in 90 MPa hydrogen gas compared to air.
2. The degradation of block boundaries due to hydrogen-enhanced plasticity-mediated decohesion, driven by cyclic plasticity ahead of the crack tip, results in cycle-dependent FCG acceleration.
3. A reduction in the cohesive strength of prior austenite grain boundaries (PAGBs) is attributed to hydrogen-enhanced decohesion (HEDE). Consequently, the hydrogen-enhanced plasticity-mediated decohesion of block boundaries, in combination with HEDE of PAGBs, accelerates FCG in high-pressure hydrogen.

CRediT authorship contribution statement

Aman Arora: Writing – original draft, Validation, Methodology, Investigation, Formal analysis, Data curation. **Akinobu Shibata:** Writing – review & editing, Visualization, Validation, Supervision, Conceptualization. **Hisao Matsunaga:** Writing – review & editing, Supervision, Resources, Project administration, Methodology, Funding acquisition, Conceptualization.

Declaration of competing interest

The authors declare that they have no known competing financial interests or personal relationships that could have appeared to influence the work reported in this paper.

Acknowledgement

This work was supported by the MEXT Program: Data Creation and Utilization Type Material Research and Development Project, Grant Number JPMXP1122684766.

Data availability

Data will be made available on request.

References

[1] Zheng J, Liu X, Xu P, Liu P, Zhao Y, Yang J. Development of high pressure gaseous hydrogen storage technologies. Int J Hydrogen Energy Jan. 2012;37(1):1048–57. https://doi.org/10.1016/j.ijhydene.2011.02.125.

[2] H. Li *et al.*, "Safety of hydrogen storage and transportation: An overview on mechanisms, techniques, and challenges," Nov. 01, 2022, *Elsevier Ltd*. doi: 10.1016/j.egyr.2022.04.067.

[3] Pu L, Yu H, Dai M, He Y, Sun R, Yan T. Research progress and application of high-pressure hydrogen and liquid hydrogen in storage and transportation. Kexue Tongbao/Chinese Science Bulletin 2022;67(19):2172–91. https://doi.org/10.1360/TB-2022-0063.

[4] H. Fukumoto, Y. Wada, H. Matsunaga, T. Sano, and H. Kobayashi, "Introduction of technical document in Japan for safe use of ground storage vessels made of low alloy steels for hydrogen refueling stations," 2018. [Online]. Available: https://proceedings.asmedigitalcollection.asme.org.

[5] A. Macadre, M. Artamonov, S. Matsuoka, and J. Furtado, "Effects of hydrogen pressure and test frequency on fatigue crack growth properties of Ni-Cr-Mo steel candidate for a storage cylinder of a 70MPa hydrogen filling station," *Eng Fract Mech*, vol. 78, no. 18, 2011, doi: 10.1016/j.engfracmech.2011.09.007.

[6] A. Shibata *et al.*, "Relationship between Three-dimensional Crack Morphology and Macroscopic Mechanical Properties of Hydrogen-related Fracture in Martensitic Steel," *ISIJ International*, vol. 64, no. 4, 2024, doi: 10.2355/isijinternational.ISIJINT-2023-316.

[7] A. Shibata, "Relationship between Hydrogen-related Fracture and Microstructure in High-strength Martensitic Steels," *Materia Japan*, vol. 61, no. 12, 2022, doi: 10.2320/materia.61.860.

[8] A. Shibata, "Hydrogen-related Fracture in Martensitic Steels," *Zairyo/Journal of the Society of Materials Science, Japan*, vol. 71, no. 8, 2022, doi: 10.2472/jsms.71.672.

[9] J. Yamabe, H. Itoga, T. Awane, T. Matsuo, H. Matsunaga, and S. Matsuoka, "Pressure Cycle Testing of Cr-Mo Steel Pressure Vessels Subjected to Gaseous Hydrogen," *Journal of Pressure Vessel Technology, Transactions of the ASME*, vol. 138, no. 1, 2016, doi: 10.1115/1.4030086.

[10] K. Ma, J. Zheng, Z. Hua, C. Gu, R. Zhang, and Y. Liu, "Hydrogen assisted fatigue life of Cr–Mo steel pressure vessel with coplanar cracks based on fatigue crack growth analysis," *Int J Hydrogen Energy*, vol. 45, no. 38, 2020, doi: 10.1016/j.ijhydene.2020.05.034.

[11] Matsunaga H, Yamabe J, Takakuwa O, Ogawa Y, Matsuoka S. *Hydrogen gas embrittlement: Mechanisms, mechanics, and design*. Elsevier 2024. https://doi.org/10.1016/c2020-0-01846-3.

[12] Li X, Zhang J, Cui Y, Djukic MB, Feng H, Wang Y. Review of the hydrogen embrittlement and interactions between hydrogen and microstructural interfaces in metallic alloys: Grain boundary, twin boundary, and nano-precipitate. Int J Hydrogen Energy Jun. 2024;72:74–109. https://doi.org/10.1016/J.IJHYDENE.2024.05.257.

[13] H. Yu *et al.*, "Hydrogen Embrittlement as a Conspicuous Material Challenge—Comprehensive Review and Future Directions," May 22, 2024, *American Chemical Society*. doi: 10.1021/acs.chemrev.3c00624.

[14] Matsuoka S, Matsunaga H, Yamabe J, Hamada S, Iijima T. Various strength properties of SCM435 and SNCM439 low-alloy steels in 115 MPa hydrogen gas and proposal of design guideline. Transactions of the JSME (in Japanese) 2017;83(854):17–00264. https://doi.org/10.1299/transjsme.17-00264.

[15] Nibur KA, Somerday BP, Marchi CS, Foulk JW, Dadfarnia M, Sofronis P. The relationship between crack-tip strain and subcritical cracking thresholds for steels in high-pressure hydrogen gas. Metall Mater Trans A Jan. 2013;44(1):248–69. https://doi.org/10.1007/s11661-012-1400-5.

[16] Ogawa Y, Nishida H, Nakamura M, Olden V, Vinogradov A, Matsunaga H. Dual roles of pearlite microstructure to interfere/facilitate gaseous hydrogen-assisted fatigue crack growth in plain carbon steels. Int J Fatigue 2022;154. https://doi.org/10.1016/j.ijfatigue.2021.106561.

[17] Redarce T, Iwata K, Ogawa Y, Tsuzaki K, Shibata A, Matsunaga H. Ausformed high-strength low-alloy steel exhibits exceptional resistance to fatigue crack-growth in high-pressure hydrogen environments. Int J Fatigue Apr. 2025;193:108814. https://doi.org/10.1016/j.ijfatigue.2025.108814.

[18] J. Yamabe, T. Matsumoto, S. Matsuoka, and Y. Murakami, "A new mechanism in hydrogen-enhanced fatigue crack growth behavior of a 1900-MPa-class high-strength steel," *Int J Fract*, vol. 177, no. 2, 2012, doi: 10.1007/s10704-012-9760-9.

[19] Setoyama A, et al. Transition mechanism of cycle- to time-dependent acceleration of fatigue crack-growth in 0.4 %C Cr-Mo steel in a pressurized gaseous hydrogen environment. Int J Fatigue Oct. 2022;163. https://doi.org/10.1016/j.ijfatigue.2022.107039.

[20] S. SURESH and R. O. RITCHIE, "GEOMETRIC MODEL FOR FATIGUE CRACK CLOSURE INDUCED BY FRACTURE SURFACE ROUGHNESS.," *METALL TRANS A*, vol. V 13A, no. N 9, 1982, doi: 10.1007/bf02644803.

[21] G. T. Gray, J. C. Williams, and A. W. Thompson, "Roughness-Induced Crack Closure: An Explanation for Microstructurally Sensitive Fatigue Crack Growth," *Metallurgical Transactions A*, vol. 14, no. 2, 1983, doi: 10.1007/BF02644220.

[22] Vasudevan AK, Kujawski D. Roughness induced crack Closure: A review of key points. Theor Appl Fract Mech 2023;125. https://doi.org/10.1016/j.tafmec.2023.103897.

[23] Okada K, Shibata A, Matsumiya H, Tsuji N. Origin of serrated markings on the hydrogen related quasi-cleavage fracture in low-carbon steel with ferrite microstructure. ISIJ Int 2022;62(10):2081–8. https://doi.org/10.2355/isijinternational.ISIJINT-2022-212.

[24] R. Pippan and A. Hohenwarter, "Fatigue crack closure: a review of the physical phenomena," Apr. 01, 2017, *Blackwell Publishing Ltd*. doi: 10.1111/ffe.12578.

[25] Toribio J, Kharin V. "On the role of plasticity-induced fatigue crack closure in high-strength steels," in Fatigue of Materials III: Advances and Emergences in Understanding -. In: *Proceedings of the 3rd Biennial Symposium, held during Materials Science and Technology 2014, MS and T*; 2014, 2014.. https://doi.org/10.1002/9781119041498.ch16.

[26] Toribio J, Kharin V. Role of fatigue crack closure stresses in hydrogen-assisted cracking. ASTM Spec Tech Publ 1999. https://doi.org/10.1520/stp15773s.

[27] Y. Murakami, T. Kanezaki, Y. Mine, and S. Matsuoka, "Hydrogen embrittlement mechanism in fatigue of austenitic stainless steels," *Metall Mater Trans A Phys Metall Mater Sci*, vol. 39 A, no. 6, 2008, doi: 10.1007/s11661-008-9506-5.

[28] S. Suresh and R. O. Ritchie, "On the influence of environment on the load ratio dependence of fatigue thresholds in pressure vessel steel," *Eng Fract Mech*, vol. 18, no. 4, 1983, doi: 10.1016/0013-7944(83)90124-8.

[29] J. Toplosky and R. O. Ritchie, "On the influence of gaseous hydrogen in decelerating fatigue crack growth rates in ultrahigh strength steels," *Scripta Metallurgica*, vol. 15, no. 8, 1981, doi: 10.1016/0036-9748(81)90275-1.

[30] Okada K, Shibata A, Sasaki T, Matsumiya H, Hono K, Tsuji N. Improvement of resistance against hydrogen embrittlement by controlling carbon segregation at prior austenite grain boundary in 3Mn-0.2C martensitic steels. Scr Mater 2023;224:Feb. https://doi.org/10.1016/j.scriptamat.2022.115043.

[31] (astm),. "ASTM E647−05 Standard test method for measurement of fatigue crack growth rates," *ASTM*. International 2014.

[32] Article KD-10, "Special requirements for vessels in high pressure gaseous hydrogen transport and storage service," *ASME Boiler and Pressure Vessel Code, Division VIII, Section 3, ASME, New York*.

[33] Si Y, Rouse JP, Hyde CJ. "Potential difference methods for measuring crack growth. A review" 2020. https://doi.org/10.1016/j.ijfatigue.2020.105624.

[34] P. Paris and F. Erdogan, "A critical analysis of crack propagation laws," *Journal of Fluids Engineering, Transactions of the ASME*, vol. 85, no. 4, 1963, doi: 10.1115/1.3656900.

[35] J. A. Ronevich, B. P. Somerday, and C. W. San Marchi, "Effects of microstructure banding on hydrogen assisted fatigue crack growth in X65 pipeline steels," *Int J Fatigue*, vol. 82, 2016, doi: 10.1016/j.ijfatigue.2015.09.004.

[36] Ogawa Y, Umakoshi K, Nakamura M, Takakuwa O, Matsunaga H. Hydrogen-assisted, intergranular, fatigue crack-growth in ferritic iron: Influences of hydrogen-gas pressure and temperature variation. Int J Fatigue 2020;140. https://doi.org/10.1016/j.ijfatigue.2020.105806.

[37] Wolf E. "The significance of Fatigue Crack Closure," in *damage Tolerance in Aircraft Structures*, ASTM STP 486., vo. American Society for Testing and Materials 1971;1971:230–42.

[38] McClung R, Newman J. Advances in Fatigue Crack Closure Measurement and Analysis: Second Volume 1999. https://doi.org/10.1520/stp1343-eb.

[39] Macha DE, Corbly DM, Jones JW. "On the variation of fatigue crack opening load with measurement location.," in *Paper* -. SESA (Society for Experimental Stress Analysis) 1979. https://doi.org/10.1007/bf02324983.

[40] Y. Xu, P. J. Gregson, and I. Sinclair, "Systematic assessment and validation of compliance-based crack closure measurements in fatigue," *Materials Science and Engineering A*, vol. 284, no. 1–2, 2000, doi: 10.1016/S0921-5093(00)00758-9.

[41] Kikukawa M, Jono M, Tanaka K, Takatani M. Fatigue crack closure behavior at low stress intensity levels. Proceedings of ICM 1976;2:254–77.

[42] Ogawa Y, et al. Fatigue crack-growth retardation after overloading in gaseous hydrogen: Revisiting the effect of hydrogen on crack-tip plastic-zone development. Mater Lett Feb. 2022;308. https://doi.org/10.1016/j.matlet.2021.131115.

[43] Sofronis P, McMeeking RM. Numerical analysis of hydrogen transport near a blunting crack tip. J Mech Phys Solids 1989;37(3):317–50. https://doi.org/10.1016/0022-5096(89)90002-1.

[44] R. A. Oriani, "The diffusion and trapping of hydrogen in steel," *Acta Metallurgica*, vol. 18, no. 1, 1970, doi: 10.1016/0001-6160(70)90078-7.

[45] M. Dadfarnia *et al.*, "Recent advances in the study of structural materials compatibility with hydrogen," *Advanced Materials*, vol. 22, no. 10, 2010, doi: 10.1002/adma.200904354.

[46] A. Turnbull, "Hydrogen diffusion and trapping in metals," 2012. doi: 10.1533/9780857095374.1.89.

[47] M. Dadfarnia, A. Nagao, S. Wang, M. L. Martin, B. P. Somerday, and P. Sofronis, "Recent advances on hydrogen embrittlement of structural materials," *Int J Fract*, vol. 196, no. 1–2, 2015, doi: 10.1007/s10704-015-0068-4.

[48] Wei FG, Tsuzaki K. "Hydrogen trapping phenomena in martensitic steels," in *gaseous hydrogen embrittlement of materials in energy technologies*. The Problem, its Characterisation and Effects on Particular Alloy Classes 2012. https://doi.org/10.1533/9780857093899.3.493.

[49] A. Nagao, C. D. Smith, M. Dadfarnia, P. Sofronis, and I. M. Robertson, "The role of hydrogen in hydrogen embrittlement fracture of lath martensitic steel," *Acta Mater*, vol. 60, no. 13–14, 2012, doi: 10.1016/j.actamat.2012.06.040.

[50] I. M. Robertson *et al.*, "Hydrogen Embrittlement Understood," *Metall Mater Trans A Phys Metall Mater Sci*, vol. 46, no. 6, 2015, doi: 10.1007/s11661-015-2836-1.

[51] R. A. Oriani and P. H. Josephic, "Testing of the decohesion theory of hydrogen-induced crack propagation," *Scripta Metallurgica*, vol. 6, no. 8, 1972, doi: 10.1016/0036-9748(72)90126-3.

[52] Djukic MB, Bakic GM, Zeravcic VS, Sedmak A, Rajicic B. "The synergistic action and interplay of hydrogen embrittlement mechanisms in steels and iron. Localized plasticity and decohesion" 2019. https://doi.org/10.1016/j.engfracmech.2019.106528.

[53] Tao P, et al. Dual-phase cohesive zone modelling and experimental validation for hydrogen-assisted cracking of 2205 duplex stainless steel. Int J Press Vessel Pip 2021;190. https://doi.org/10.1016/j.ijpvp.2020.104296.

[54] T. Chen, T. Chiba, M. Koyama, A. Shibata, E. Akiyama, and K. Takai, "Hierarchical Characteristics of Hydrogen-Assisted Crack Growth and Microstructural Strain Evolution in Tempered Martensitic Steels: Case of Quasi-cleavage Fracture," *Metall Mater Trans A Phys Metall Mater Sci*, vol. 52, no. 10, 2021, doi: 10.1007/s11661-021-06423-1.
[55] Yoder GR, Cooley LA, Crooker TW. On Microstructural Control of Near-Threshold Fatigue Crack Growth in 7000-Series Aluminum Alloys. Scr Metall 1982;16:1021–5.
[56] Jono M, Song J, Ohgaki M. Fatigue Crack Growth and Crack Closure Behavior of Structural Materials. J Soc Mater Sci, Jpn 1984;33:468–74.
[57] Birnbaum HK, Sofronis P. Hydrogen-enhanced localized plasticity-a mechanism for hydrogen-related fracture. Mater Sci Eng A 1994;176(1–2):191–202. https://doi.org/10.1016/0921-5093(94)90975-X.
[58] Djukic MB, Zeravcic VS, Bakic GM, Sedmak A, Rajicic B. Hydrogen damage of steels: A case study and hydrogen embrittlement model. Eng Fail Anal 2015;58:485–98. https://doi.org/10.1016/j.engfailanal.2015.05.017.
[59] Laird C. The Influence of Metallurgical Structure on the Mechanisms of Fatigue Crack Propagation. ASTM Spec Tech Publ 1967. https://doi.org/10.1520/STP47230S.
[60] R. M. N. PELLOUX, "Mechanism of Formation of Ductile Fatigue Striations," *Trans ASM*, vol. 62, pp. 281–285, 1969, Accessed: Jul. 23, 2024. [Online]. Available: https://cir.nii.ac.jp/crid/1570572699145602816.bib?lang=en.
[61] P. Neumann, "New experiments concerning the slip processes at propagating fatigue cracks-I," *Acta Metallurgica*, vol. 22, no. 9, 1974, doi: 10.1016/0001-6160(74)90071-6.
[62] Bichler C, Pippan R. Direct observation of the formation of striations. ENGINEERING AGAINST FATIGUE 1999.
[63] H. NISHIKAWA, Y. ODA, Y. TAKAHASHI, and H. NOGUCHI, "Microscopic Observation of the Brittle-Striation Formation Mechanism in Low Carbon Steel Fatigued in Hydrogen Gas (TEM and EBSD Observation Corresponding to Fractography)," *Journal of Solid Mechanics and Materials Engineering*, vol. 5, no. 4, 2011, doi: 10.1299/jmmp.5.179.
[64] S. Matsuoka, H. Tanaka, N. Homma, and Y. Murakami, "Influence of hydrogen and frequency on fatigue crack growth behavior of Cr-Mo steel," *Int J Fract*, vol. 168, no. 1, 2011, doi: 10.1007/s10704-010-9560-z.
[65] S. P. Lynch, "Hydrogen embrittlement (HE) phenomena and mechanisms," 2011. doi: 10.1533/9780857093769.1.90.
[66] Nagao A, Dadfarnia M, Somerday BP, Sofronis P, Ritchie RO. Hydrogen-enhanced-plasticity mediated decohesion for hydrogen-induced intergranular and 'quasi-cleavage' fracture of lath martensitic steels. J Mech Phys Solids 2018;112. https://doi.org/10.1016/j.jmps.2017.12.016.